Research Square

Preprints are preliminary reports that have not undergone peer review.
They should not be considered conclusive, used to inform clinical practice,
or referenced by the media as validated information.

Joint aerothermodynamic yield architecture : an open-source tool for martian atmospheric reentry vehicle with interlinked multi-physics modeling

Sanjay Lakshminarayana

sanjaylakshminarayana@outlook.com

Department of Space Technology, AGH University of Kraków, al. Adama Mickiewicza 30, Kraków, 30-059, Poland

Shreyas Srivatsa

Department of Space Technology, AGH University of Kraków, al. Adama Mickiewicza 30, Kraków, 30-059, Poland

Tadeusz Uhl

Department of Space Technology, AGH University of Kraków, al. Adama Mickiewicza 30, Kraków, 30-059, Poland

Research Article

Keywords: AUSM flux, multi-physics, mars re-entry, TPS modeling

Posted Date: May 22nd, 2026

DOI: https://doi.org/10.21203/rs.3.rs-9780343/v1

License: This work is licensed under a Creative Commons Attribution 4.0 International License.
Read Full License

Additional Declarations: The authors declare no competing interests.

Joint aerothermodynamic yield architecture : an open-source tool for martian atmospheric reentry vehicle with interlinked multi-physics modeling

Sanjay Lakshminarayana[1,2*], Shreyas Srivatsa[2,3] and Tadeusz Uhl[2,3]

[1,2,3*]Department of Space Technology, AGH University of Kraków, al. Adama Mickiewicza 30, Kraków, 30-059, Poland.

*Corresponding author(s). E-mail(s): sanjaylakshminarayana@outlook.com;
Contributing authors: sshreyas@agh.edu.pl; tuhl@agh.edu.pl;

Abstract

The Martian atmosphere, which is composed of 95% carbon dioxide (CO2), a surface pressure of approximately 7 millibar and a density of 0.020 kg/m^3, creates a challenging scenario for the design of the re-entry capsule. To date, a total of nine missions have achieved success in landing and operating on the surface of Mars. The re-entry flight data and accurate atmospheric models are not widely available, which hinders the development of computational tools capable of accurately predicting and modeling the aero-fluid loads and thermal protection system (TPS). Although there are specific tools developed by various space agencies that are used for such scenarios, these tools are often limited in scope, focusing on a single aspect of the re-entry process. Calculations such as trajectory analysis, radiative ray-tracing, TPS sizing often exceed the capabilities of these tools, necessitating linking with external tools to achieve a comprehensive analysis. The distribution of licenses is subject to stringent regulations and their application is constrained by specific criteria. In light of the absence of a distinctive open-source suite for simulating Mars re-entry trajectories, it is imperative to explore alternative approaches. This paper presents the joint aero-thermodynamic yield architecture (JAYA), an opensource, tightly coupled trajectory-CFD-fluid structure interaction-TPS framework for Martian atmospheric entry capsules. JAYA demonstrates high degree of accuracy of up to second order in predicting the trajectory and first order accuracy in mechanical loading, with non-linear fluid loads and TPS ablation rates. This tool also offers a high degree of flexibility by providing the possibility of incorporating correlated parameters and inputs from

flight data. Finally, a demonstration use-case is presented that utilizes the results for the Mars science laboratory–class entry scenario reproducing key entry events including peak heating, peak deceleration and TPS mass loss.

Keywords: AUSM flux, multi-physics, mars re-entry, TPS modeling

A TOTAL of nine Mars landing with surface operations missions have been successful with mission failure probability of greater than 50% [1][2]. The aero-thermal environment during Martian atmospheric entry poses significant design challenges, with peak heat fluxes exceeding $200\,\mathrm{W\,cm^{-2}}$ and surface temperatures approaching 2200 K. Accurate prediction of these environments is critical for thermal protection system (TPS) sizing and mission success [3] [4]. The list of nine missions along with the various methods used for the missions and the mathematical models incorporated are listed in the Table 1.

As listed in Table 1, among the nine successful NASA Mars surface missions, Pathfinder, MER and Phoenix missions integrated high-fidelity trajectory simulation, monte carlo dispersion analysis and multi-body lander dynamics while rest used modified apollo software. This finally guided lifting entry with advanced entry guidance, range trigger and terrain-relative navigation for landing, flight-data-driven reconstruction of atmosphere, aerodynamics and aerothermodynamics using instrumentation such as MEDLI/MEDLI2 and reconstruction frameworks such as MEADS for MSL and Mars 2020. Across these missions, the core model classes consistently include trajectory and navigation filter models, atmospheric uncertainty and density profile models, hypersonic and supersonic aerodynamic coefficient databases, aero-heating models including CFD and TPS response for later missions. It includes mechanical load models for deceleration, touchdown performance with increasing reliance on post-flight telemetry and sensor-informed reconstruction to validate pre-flight predictions and reduce EDL uncertainty [3] [5] [8][9][10][11][12][13].

For MSL which is the heaviest and highest aerodynamic load bearing re-entry mars capsule to date, trajectory was developed using modified apollo flight proven entry terminal point controller (ETPC) algorithm. It provided trajectory predictions especially with the uncertainties and unknowns for landing taken into account. Computational model developed for this particular mission case, namely the langley aero-thermodynamic upwind relaxation algorithm (LAURA) and data-parallel line relaxation (DPLR). LAURA is a three-dimensional geometry capable second-order finite volume element solver which is suitable for high enthalpy flow that encapsulates chemical non-equilibrium for the atmosphere composition and TPS design for wide range of re-entry cases. LAURA has been extensively used to assess aero-thermal environments encountered during entry, descent, and landing applications. LAURA solves the Navier–Stokes equations using a cell-centered formulation on structured, multi-block grid systems. The code incorporates a robust set of state-of-the-art modeling capabilities for high-energy flow phenomena, including shock-layer radiation, surface ablation and species ionization. DPLR is a high performance CFD code that

Table 1: Mars surface landing missions and the Entry, Descent, and Landing (EDL) tools used.

Mission	**Tools used [5][6][7]**	**Mathematical concepts incorporated**
Viking 1 (1976)	Autonomous onboard entry navigation and guidance, Viking-era aerodynamic/heating ground-test campaigns.	Trajectory: autonomous entry navigation and guidance functions. Fluid/Thermal: aerodynamic coefficients vs. Mach, stability derivatives, stagnation heating/pressure histories, and aeroshell heating distributions (test & analysis). Mechanical: entry and terminal descent performance characterization from EDL heritage.
Viking 2 (1976)	Same Viking navigation tool-chain and aerodynamic/heating characterization approach as Viking 1.	Same modeling classes as Viking 1.
Mars Pathfinder	Flight software parachute-deploy timing logic, simulation suite including 6-degree-of-freedom (DOF) program to optimize and simulate trajectories (POST), atmospheric entry program (AEP), and ADAMS multi-body dynamics.	Fluid/Thermal: atmospheric model updates in simulations. Mechanical: parachute and lander multi-body dynamics (ADAMS), impact modeling.
MER-A Spirit (2004)	POST and atmospheric entry/powered landing (AEPL) trajectory propagation codes, Monte Carlo dispersion analysis, shared aerodynamics database for MER.	Trajectory: 6DOF→3DOF transition analyses, independent code cross-checks, landing ellipse prediction. Fluid/Thermal: hypersonic/supersonic aerodynamics database with atmospheric uncertainty modeling. Mechanical: parachute, lander drag, and performance dispersions in Monte Carlo. Tools used—POST + AEPL + Monte Carlo + shared aero database.
MER-B Opportunity (2004)	Same MER EDL analysis toolchain as Spirit.	
Phoenix (2008)	POST2 EDL simulation, empirical parachute inflation model, simplified wrist-mode torque model in POST-2, with separate multi-body Phoenix simulation for parachute and capsule dynamics.	Fluid/Thermal: aero-heating metrics with peak heat rate tracked in Monte Carlo. Mechanical: parachute dynamics (single-body vs. multibody), descent/touchdown constraints.
MSL Curiosity (2012)	End-to-end EDL simulations; entry guidance (ETPC), MEDLI heatshield instrumentation, MEADS/flush-air-data-style reconstruction, LAURA/DPLR CFD, and FIAT TPS thermal-response reconstruction.	Fluid/Thermal: CFD-based aerothermodynamics, boundary-layer transition assessment, TPS response FIAT using MEDLI pressures/temperatures. Mechanical: EDL performance metrics and chute/powered-descent event-sequencing loads.
InSight (2018)	POST2 end-to-end performance simulation, post-flight reconstruction using Kalman filtering, onboard MIMU and radar-altimeter data streams.	Fluid/Thermal: trajectory and atmosphere reconstruction with heritage methods. Mechanical: sensor uncertainty models propagated in reconstruction and performance assessment.
Mars 2020 Perseverance (2021)	POST2 as prime EDL performance simulation, DSENDS independent verification/reference simulation, entry guidance (ETPC) + Range Trigger + Terrain-Relative Navigation (TRN/LVS), MEDLI2 instrumentation, and MEADS-style trajectory/aero/atmosphere reconstruction.	Fluid/Thermal: MEDLI2 pressure/temperature/heat-flux instrumentation enabling aero/atmosphere/aerothermal reconstruction and CFD-to-flight comparisons. Mechanical: EDL sequence performance, loads, and landing-accuracy verification via simulation + reconstruction.

simulates hypersonic flow and aero-thermal loads making it suitable of re-entry vehicle design. DPLR with transitional modeling capability is built for higher resolution of wall fluxes, especially for complex geometries. DPLR is a structured, multi-block finite-volume solver for the Navier–Stokes equations that supports non-equilibrium gas-phase chemistry, boundary-layer modeling, and turbulence. Its numerical formulation uses data-parallel line relaxation for implicit time advancement, enabling efficient solution of large, stiff systems typical of high-enthalpy entry flows. Physical modeling capabilities of DPLR, including finite-rate chemistry, vibrational and rotational non-equilibrium, multiple turbulence models and support for laminar-to-turbulent transition specification. It can also be loosely coupled with external software's like HARA (Hypersonic Air Radiation Algorithm) for radiative ray tracing calculation.Table 2 list key physics, architecture differences and highlights between LAURA and DPLR also in combination with HARA. The tool coupling between DPLR and HARA provided detailed shock-layer radiation calculations, enabling quantification of radiative heating contributions and associated uncertainties for the high-energy Mars entry conditions. Ablative TPS sizing is performed using the fully implicit ablation and thermal response program (FIAT) which solves uni-dimensional energy transfer for multilayered TPS accounting both ablation and decomposition. The tool balances internal energy and decomposition with surface energy balance equations then coupling it with thermochemical equations. Thus providing detailed analogy into TPS ablation mass, temperature and fluxes at interfaces, depth of pyrolysis and ablation. The TPS uses trajectory data from ETPC, aerothermal data from LAURA, DPLR combined and then FIAT was able to assess the scaling and uncertainty quantification of TPS behavior[9][11] [14] [15] [16] [17] [18].

Also, computational tools like DPLR complement experimental and flight data to provide comprehensive predictions of heating, pressure, and flow field properties for earth and planetary entry vehicles. The LAURA, HARA and DPLR computational tools played a central role in the aero-thermodynamic design and risk reduction of the MSL entry system. LAURA and DPLR were used extensively to predict the hypersonic flow field, surface pressure and convective heating environments along the MSL entry trajectory. Thus, supporting the development of the thermal protection system under unprecedented mechanical, thermal and mass constraints [19][20][15][21][22].

MSL flight data indicates that the Boundary Layer Transition (BLT) will occur prior to the peak heat event during re-entry. The heat-shield design uniquely accounted for turbulent flow effects evaluated in combination with LAURA, DLPR along the TPS design trajectory. Temperature on the heat-shield was measured with 7 positions on its fore-body, yielded heating profiles that agreed well with flight measurements prior to peak heat event during re-entry. The re-entry was at 16 degree angle of attack, with L/D Ratio of 0.24, ballistic coefficient of 140 kg/ m^2 and highest ever re-entry mass of 3257 kg. It's unprecedented aerodynamic, mechanical, thermal and mass constraints establish it as a suitable foundation for advancing multiphysics tools for future Mars entry TPS development. The tool which enable independent evaluation of tolerance and uncertainty for wide range of re-entry conditions in the view of future mars

Table 2: Comparison of LAURA, DPLR, and LAURA coupled with HARA relevant to hypersonic aerothermodynamics and TPS analysis.

Comparison aspect	LAURA	DPLR [23][24][20]	LAURA + HARA [25]
Primary development heritage	NASA Langley aerothermodynamics codebase	NASA Ames hypersonic continuum CFD codebase	Langley LAURA flow + HARA radiation used together for aero-radiation environments.
Formulation / grid class	Cell-centered, structured multi-block finite volume.	Generalized multi-block finite volume; requires point-matched structured grids.	Same LAURA flow field discretization, with radiation source terms/heating supplied via HARA.
Spatial accuracy & inviscid flux	Formal 2nd-order; based on an upwind relaxation algorithm and uses TVD concepts.	3rd-order modified Steger-Warming Euler fluxes; viscous fluxes 2nd-order central.	Same as LAURA for the flow-field; radiation adds additional coupled source terms (can affect temperatures/chemistry)
Implicit / time advancement approach	Relaxation-based marching with options including point-implicit and line-implicit (line relaxation) controls.	Dual-time stepping (2nd-order in time) and Data-Parallel Line Relaxation for implicit advancement.	Same LAURA flow solution strategy, but with tighter coupling to radiation and ray-tracing routines integrated for practical runs
Parallel execution model	MPI build available (separate executable); newer work improves multiple MPI ranks per block.	Designed as massively parallel; requires MPI even on single processor.	Adds significant radiation workload, but HARA has GPU/OpenACC acceleration to reduce line-of-sight cost.
Shock/grid adaptation features	Shock-alignment/adaptation workflow.	Built-in routine to adapt grid to bow shock location.	Same LAURA mesh strategy; additionally supports radiation evaluations across the surface.
Turbulence + transition handling	Focus on algebraic RANS models with multiple transition options and transition maps.	Multiple turbulence models (Baldwin-Lomax, Spalart-Allmaras, SST) and user-specified transition maps.	Same LAURA turbulence/transition set; LAURA/HARA work also highlights improved control of transition specification for aero thermal studies.
Thermochemistry	Designed for high-energy reacting flows; emphasizes thermochemical non-equilibrium capability.	Supports finite-rate kinetics and thermal/chemical non-equilibrium; includes ionized flow physics.	Same LAURA high-T flow models, with radiation feedback; LAURA/HARA highlights shock-layer radiation and ionization among modeled phenomena
Radiation capability (baseline)	Typically used for convective aerothermodynamics without radiation coupling (radiation is a separate workflow).	Fully coupled optically thin radiation capability and hooks for loose coupling to radiation/material response codes.	HARA evaluates shock-layer radiation and supplies radiative source terms + surface radiative heating (beyond optically thin simplifications)
Radiation transport + design-grade extras	Not applicable unless radiation coupling is enabled.	Radiation coupling exists; transport approach depends on coupling and radiation tool chain used.	Mature ray tracing, opacity binning, and automated UQ workflow; GPU speedups enable routine ray tracing

missions[26][3] [13][14][27] [28] [29] [30][19].

Currently, there is no multi-physics software that directly couples trajectory analysis, CFD, fluid-structure interaction (FSI), TPS studies. Furthermore, there is no such open source tool that can be compared to LAURA, DPLR, FIAT in terms of TPS design estimation. The possibility to evaluate TPS sizing and quantify uncertainty in its performance is not possible without linking handful of unique solver tools. This paper proposes a new tool in development, based on a Navier–Stokes solver that computes fluid–geometry interaction and near-wall heat fluxes for the modeled trajectory state and corresponding TPS response. The fully coupled solver, called joint aero-thermodynamic yield architecture (JAYA), provides TPS behavior and sizing. JAYA iteratively calculates the trajectory using fourth-order Runge-Kutta time integration while aerodynamic forces and near-wall convective heating are obtained directly from a finite-volume Navier-Stokes solver on a body-fitted, axisymmetric structured grid. Inviscid fluxes are evaluated using an advection upstream splitting method (AUSM)-type splitting method blended with a Rusanov flux for robustness across shocks and strong gradients. Viscous terms employ central differencing with an algebraic mixing-length eddy-viscosity augmentation and an altitude-based turbulence switch. The aero-thermal interface computes wall heat flux from near-wall temperature gradients and couples it to a finite-rate, TPS response model. While, temperature-dependent properties such as radiative losses, recession, and mass-loss feedback to the trajectory.

Finally, the paper structure is provided henceforth. The materials and methodology section describes the MSL test case implementation with the new tool with a description of coupling between CFD, FSI, TPS, aero-thermal heating, and trajectory module. The algorithm implemented with their formulae and the equations used to build the tool are provided. The results section presents the outputs in terms of trajectory, aero-thermal profiles, and CFD outcomes. The conclusion outlines the advantages and limitations of the proposed simulation suite and the directions for future work.

1 Materials and Methodology

The test case utilized for input serves as a two-dimensional representation of MSL, illustrating the geometry of the vehicle. The atmosphere model is taken to be from Mars-GRAM 2010 (Mars Global Reference Atmospheric Model) with parameterized surrogate for landing site as Gale Crater. Further Table 3 represents the initial conditions defined for the simulation with Lift to Drag (L/D) taken as constant 0.24. MSL mass baseline at the beginning of the re-entry simulation is 3300 kilogram with flight angle of 16 degree and at 125 kilometer from the Martian surface. Figure 1 illustrates the sequence of events part of the simulation. The MSL is assumed to be at the entry interface with de-spin , cruise balance already performed and at entry altitude, CFD and TPS solvers remain active from 80 km altitude until parachute open event. This paper discusses results particular to this phase of flight [29][19][31][32].

The simulation framework as shown in Figure 2 consists of mainly three coupled computational components, which are

1. trajectory dynamics solver
2. Aero-thermodynamic CFD solver

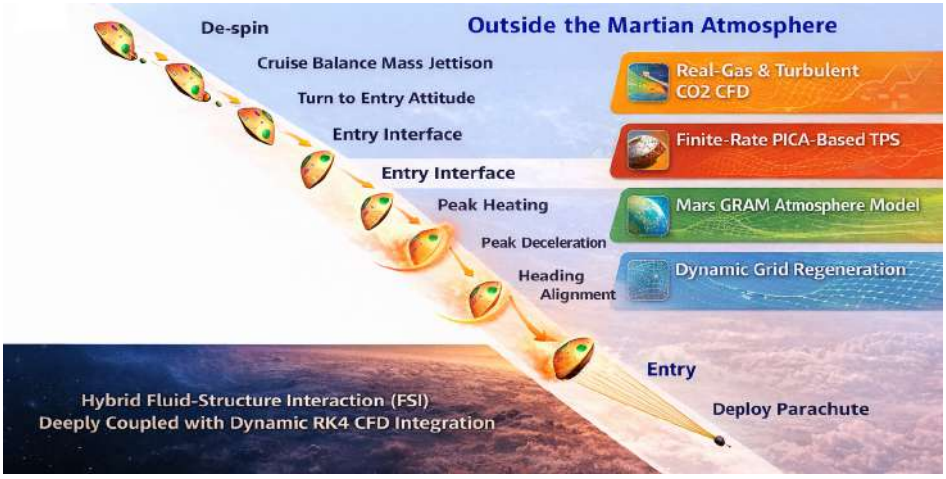


Fig. 1: Simulated mission timeline (generated using AI tool Gemini)

Table 3: Test-case setup for MSL trajectory simulation used in JAYA.

Parameter	**Description** [2][3][31]
Test case input	2D equivalent of MSL representing the vehicle geometry
Atmospheric model	Mars-GRAM 2010
Landing site (parameterization)	Gale Crater
Numerical integration method	Runge–Kutta method
Initial altitude	125 km
Initial velocity	5800 m/s
Initial flight path angle	16°
Initial mass	3300 kg, rounded off (MSL $\sim$ 3257 kg)
L/D ratio	0.24

3. TPS thermal response solver

These components are advanced in a time-synchronous manner using a shared global time step, with sequential two-way coupling enforced at each step. The coupling between the trajectory solver and the CFD solver provides the freestream conditions required to define the outer boundary of the computational flow domain. At the beginning of each global time step, the trajectory solver advances the state of the vehicle using the current aerodynamic forces and gravitational acceleration. From the updated flight state and the Mars atmospheric model, the instantaneous freestream velocity, density, temperature, Mach number, and flight-path angle are computed. These quantities are supplied directly to the CFD solver and are used to prescribe the far-field

boundary conditions, ensuring thermodynamic and kinematic consistency between the trajectory solution and the resolved flow-field. Following specification of the freestream conditions, CFD solver advances the compressible Navier–Stokes equations on a body-fitted structured mesh using a finite volume formulation. Inviscid fluxes are evaluated using an AUSM-type flux splitting scheme with pressure-based blending to a Rusanov flux in regions of strong gradients, while viscous fluxes are computed using central differencing with an effective viscosity that includes an algebraic mixing-length turbulence augmentation. After the flow field solution is updated, surface pressure and wall shear stress distributions are integrated over the vehicle surface to obtain net aerodynamic forces. These forces are returned to the trajectory solver and used in the subsequent update of the equations of motion, thereby closing the aerodynamic feedback loop[33–35].

The interface between the CFD solver and TPS solver governs the transfer of aerothermal loading. After completion of the CFD solution at each global time step, the local convective wall heat flux is computed from the near-wall temperature gradient using the effective gas thermal conductivity. A calibrated reduction factor is applied to account for surface roughness effects. The resulting heat-flux distribution is mapped directly onto the TPS surface discretization and applied as a boundary condition for the TPS thermal solver. The TPS solver advances the transient one-dimensional heat conduction equation within the material over the same global time interval, accounting for internal conduction, applied aerodynamic heating, and surface radiative losses. Material properties are treated as temperature-dependent, and surface recession is computed using an effective heat of ablation model based on the local net heat flux. Ablation is represented through an energy balance consistent with the implemented material response model. Surface recession predicted by the TPS solver is fed back to the CFD solver through a geometry update procedure. Local recession distances are converted into normal displacements of the surface nodes based on the computed ablation rate and global time step. The CFD surface mesh is updated accordingly, and interior grid points are smoothly displaced using a wall-distance-based damping function to preserve mesh quality and avoid excessive cell skewness. This geometric feedback ensures that changes in vehicle shape due to ablation directly influence subsequent aerodynamic forces and surface heating predictions. Mass coupling between the TPS and trajectory solvers is enforced by integrating the surface mass-loss rate over the vehicle surface at each time step. The resulting mass decrement is subtracted from the vehicle mass used in the trajectory equations of motion, ensuring consistency between TPS erosion, vehicle inertia, and ballistic performance throughout the entry simulation[36][28].

1.1 Algorithm

The algorithm implements a fully coupled trajectory–CFD–TPS–FSI framework for Mars entry vehicles, integrating flight dynamics, aerothermodynamics, thermal protection, and structural response in a time-synchronous manner. At each global time step, atmospheric properties are obtained from Mars-GRAM [37], aerodynamic forces and surface heating are computed using the Navier–Stokes equations with the AUSM$^+$

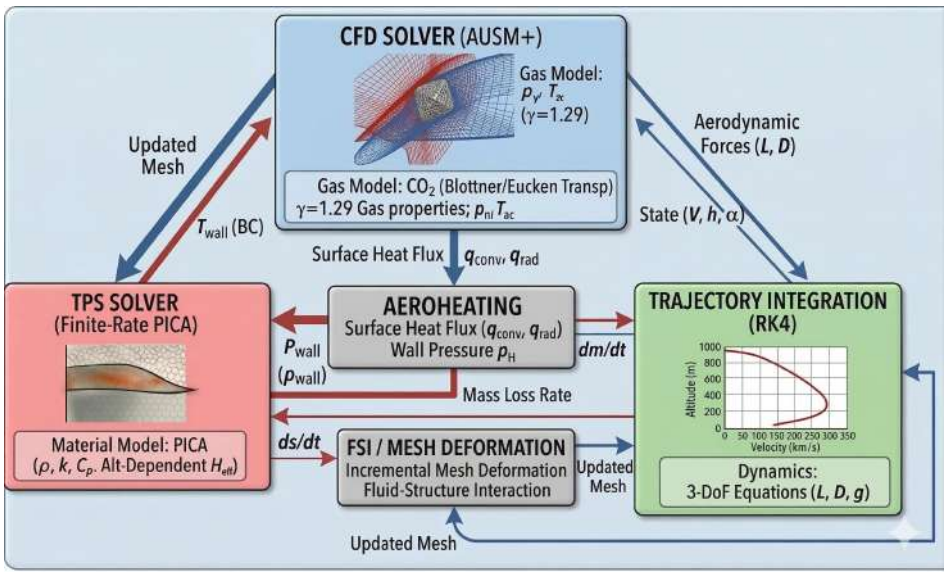


Fig. 2: JAYA — Joint Aerothermodynamic Yield Architecture Interfaces chart

flux scheme [38], and transient TPS response—including ablation and heat conduction—is solved. Surface recession and mass loss are fed back to both the CFD and trajectory solvers while structural deformation from FSI is applied to update the mesh. Runge–Kutta integration advances vehicle motion, preserving aero-thermodynamic consistency [39, 40].

The algorithm evaluates a candidate entry trajectory by integrating the vehicle state forward in time while updating (i) the atmospheric properties from an engineering atmosphere model, (ii) aerodynamic loads from compressible flow simulation, and (iii) TPS heating/ablation and the resulting mass/geometry changes. The overall structure is a single-pass, explicit coupling executed at each time step $\triangle$t. The algorithm begins by setting the simulation clock and state: Initialize time t=0, step $\triangle$t, initialize y_0, and a maximum integration time t_{max}. Initial mass and parameters from Table 3 is considered as initial conditions, stagnation-point heating coefficient K is also set. At each step, freestream properties are obtained from Mars-GRAM. Then, implement the CFD-based aerodynamic model when h ¡ 80 kilo meter. The navier-stokes conservative form equation is implemented with FVM. The inviscid flux across control-volume faces is computed using an AUSM + type flux splitting scheme. The aerodynamic drag is computed by integrating the surface pressure and shear projected along the freestream direction. The computed drag then feeds the trajectory EOM as the dominant aerodynamic force component.

The algorithm computes stagnation-point convective heating using a correlation that scales with atmospheric density, velocity and nose radius. It includes an enthalpy-based correction to represent the reduced driving potential for heat transfer as the wall state approaches the external flow state. A total heating rate is then formed by

Algorithm 1 JAYA architecture algorithm

Initialize time $t = 0$, time step Δt, and maximum time $t_{\max}$ Initialize trajectory state vector

$$\mathbf{y}_0 = [h_0,\ V_0,\ \gamma_0,\ s_0]$$

Set initial vehicle mass $m_0 = 3300$ kg Set stagnation-point heating coefficient $K = 2.0 \times 10^{-4}$ $h > 0$ $t < t_{\max}$ **Atmospheric Environment Evaluation** Obtain freestream density ρ_∞, temperature T_∞, and pressure P_∞ from Mars-GRAM **Aerodynamic Modeling** $h \leq 80$ km Solve compressible Navier–Stokes equations using FVM with AUSM$^+$ flux scheme Obtain surface pressure p and wall shear stress τ Compute aerodynamic drag:

$$F_{\text{drag}} = \int_A (p\, n_x + \tau\, t_x)\ dA$$

Aerothermal Heating Assessment Compute stagnation-point convective heating:

$$q_{\text{stag}} = K \sqrt{\frac{\rho_\infty}{R_n}} V^3 \left(1 - \frac{H_w}{H_e}\right)$$

Evaluate total heating:

$$q_{\text{total}} = q_{\text{stag}} + q_{\text{rad}} + 700$$

Thermal Response and Mass Evolution $T_{\text{surf}} > 1000$ K Compute mass loss rate:

$$\dot{m} = \frac{q_{\text{total}}}{H_{\text{eff}}(h)}$$

Update vehicle mass:

$$m \leftarrow m - \dot{m}\, \Delta t$$

Compute surface recession rate:

$$\dot{s} = \frac{\dot{m}}{\rho_{\text{char}}}$$

Trajectory and Geometry Update Propagate trajectory state vector $\mathbf{y}$ using fourth-order Runge–Kutta integration Apply incremental mesh deformation based on surface recession rate $\dot{s}$ Update time: $t \leftarrow t + \Delta t$

adding a radiative heating contribution and an additional constant term, which should be interpreted and documented in the paper as bias correction. Thermal response and mass evolution are handled using a threshold logic intended to represent the onset of significant TPS ablation. When the surface temperature exceeds a prescribed limit of 1000 K, the algorithm converts the computed total heating into an effective mass loss rate using a lumped effective heat of ablation parameter. The vehicle mass is then reduced accordingly over the time step and surface recession rate is computed using a representative ablator density. This recession rate is subsequently used to update the entry body geometry, reflecting TPS material removal and its effect on subsequent aerodynamics and heating. Finally, the algorithm updates the trajectory state. It uses the current forces and updated mass properties to advance altitude, velocity,

flight-path angle and downrange distance. After the propagation, the surface mesh is incrementally deformed based on the computed recession, ensuring that changes in nose radius and shape feed back into the next time step's aerodynamic and heating calculations. Time is then advanced and the loop repeats.

1.2 Governing Equations and Numerical Methodology

The governing equations are divided into trajectory equations for motion of the MSL, meshing equations used for mesh deformation update performed for every iteration, CFD governing equations with finite volume method (FVM) for TPS behavior, flux and stress calculations. The assumed initial conditions, boundary conditions for wall, along the symmetric axis and the far field parameters are described.

1.2.1 Trajectory Equations of Motion

The vehicle trajectory is modeled as a planar point-mass system with state vector. The altitude, h in meters is computed using equation 1, velocity V in meters per second is computed using equation 2, flight path angle representing the angle between the velocity vector and the local horizontal γ in degrees is computed using equation 3 and downrange horizontal distance covered along the surface s in meters, using equation 4. Where, drag D in Newton is computed using equation 5. L is lift obtained using equation 6.

$$\mathbf{y} = \begin{bmatrix} h & V & \gamma & s \end{bmatrix}^T$$

The governing equations of motion are equations (1) (2) (3) and (4),

$$\frac{dh}{dt} = V \sin\gamma, \tag{1}$$

$$\frac{dV}{dt} = -\frac{D}{m} - g(h)\sin\gamma, \tag{2}$$

$$\frac{d\gamma}{dt} = \frac{L}{mV}\cos\phi - \frac{g(h)}{V}\cos\gamma + \frac{V\cos\gamma}{R_p + h}, \tag{3}$$

$$\frac{ds}{dt} = V\cos\gamma, \tag{4}$$

with gravitational acceleration with R_p as Mars radius = 3389.5×10^3 m, h is altitude in meters at time t in seconds, $g_0 = 3.71$ m/s^2, $g(h)$ is acceleration due to gravity as function of height in meters per second $\times$ second,

$$g(h) = g_0 \left(\frac{R_p}{R_p + h}\right)^2$$

Aerodynamic forces are obtained from equation (5) and Equation (6) by surface (S) integration of static pressure p in pascal, normal force n along x and y and Shear

stress acting on the surface in pascal as τ, with L being total lift and Total Drag D in Newton,

$$D = \int_S (pn_x + \tau_x)\, dS \tag{5}$$

$$L = \int_S (pn_y + \tau_y)\, dS \tag{6}$$

1.2.2 Computational Mesh

A body-fitted structured mesh is generated in axisymmetric coordinates (x, r). Let the surface be parameterized by arc length s given by,

$$\mathbf{x}_s(s) = [x(s), r(s)]$$

Surface normals are given by,

$$\mathbf{n}_s = \frac{1}{\sqrt{(x_s')^2 + (r_s')^2}} \begin{bmatrix} -r_s' \\ x_s' \end{bmatrix}$$

where x_s and r_s is position vectors of the vehicle surface coordinates. The outer boundary is defined by normal extrusion:

$$\mathbf{x}_{\text{out}}(s) = \mathbf{x}_s(s) + \delta \left[1 + 1.2 \left(\frac{r}{R_b} \right)^{1.5} \right] \mathbf{n}_s$$

where δ is a small distance increment for the initial normal extrusion, R_b is characteristic length of the vehicle in meters, n_s is surface normal vector calculated via arc length parametrization in meters. Wall-normal clustering is applied using,

$$\eta_j = \left(\frac{j}{N_j - 1} \right)^{2.5}$$

with physical coordinates

$$\mathbf{x}(i, j) = (1 - \eta_j)\mathbf{x}_s(i) + \eta_j \mathbf{x}_{\text{out}}(i)$$

where n_j is non-dimensional grid clustering parameter in the wall-normal direction, N_j is total number of grid points in the normal direction, $\boldsymbol{x}_s$ is position vector of the vehicle surface coordinates.

1.2.3 CFD Governing Equations

The compressible Navier-Stokes equations are solved in integral finite-volume form which defines the flux rate of change of conserved quantity, $\boldsymbol{U}$, inside a control volume, V equals the net flux through its closed surface,S. ρE represents the total energy per

unit volume, n is the unit normal to the surface at that point, F_c is convective or inviscid flux and F_v is viscous flux,

$$\frac{d}{dt}\int_V \mathbf{U} dV + \oint_S (\mathbf{F}_c - \mathbf{F}_v)\cdot \mathbf{n}\, dS = 0 \tag{7}$$

with conserved variables given by,

$$\mathbf{U} = \begin{bmatrix} \rho \\ \rho u \\ \rho v \\ \rho e_t \end{bmatrix}, \quad e_t = C_v T + \frac{1}{2}(u^2 + v^2)$$

where U is Conservative variable vector, e_t is total energy per unit mass in joule per kilogram, ρ is atmospheric density in kilogram per meter cube, T is the static temperature in kelvin, V is volume in m^3, u, v are velocity component along x, r axes.

1.2.4 Finite Volume Discretization

Finite volume dV is discretized as single grid cell (i, j), the rate of change of the conserved quantity inside that cell is determined by the sum of fluxes through the cell faces given by equation 8,

For cell (i, j):

$$\frac{d(\mathbf{U}_{ij}\Delta V_{ij})}{dt} = -\sum_f \left(\mathbf{F}_f^{\text{inv}} - \mathbf{F}_f^{\text{vis}}\right)\Delta A_f. \tag{8}$$

where, (i, j) cell indices along (x,y) direction indicating the 2D mesh, U_{ij} and V_{ij} represent the cell averaged conservative variable and volume of the cell, together they represent the total amount of conserved quantity inside each cell. $\sum_f$ represents the sum of fluxes over all the 6 faces of the cell since the mesh is 2D. F_f^{inv} is the inviscid flux which is evaluated in normal direction to the face of each cell. F_f^{vis} captures flux due to fluid flow and diffusion effects in normal direction to the face of each cell. A_f is area of each face of the cell,

1.2.5 Inviscid Fluxes

Inviscid transport flux are computed using an AUSM scheme with Rusanov blending used when the solver is unstable. F^{inv} inviscid numerical flux at face, F_{AUSM} is the AUSM numerical flux, F_{RUS} rusanov numerical flux, ω bleeding coefficient,

$$\mathbf{F}^{\text{inv}} = (1-\omega)\mathbf{F}_{\text{AUSM}} + \omega\mathbf{F}_{\text{RUS}},$$

where

$$\omega = \min\left(1, 10\frac{|p_R - p_L|}{p_R + p_L}\right)$$

p_L and p_R is pressure on the left and right face of the cell. ω acts as a sensor which captures shocks by indicating through the pressure based discontinuities. This term

during smooth flow discrepancies capture shocks at high accuracy with small pressure jumps i.e, $\omega \approx 0.05$ and Rusanov indicates higher accuracy with $\omega \approx 1$ with strong pressure jump.

AUSM+ flux is given by,

$$\mathbf{F}_{\text{AUSM+}} = a_f \left[M^+(M_L) \begin{bmatrix} \rho_L \\ \rho_L u_L \\ \rho_L v_L \\ \rho_L H_L \end{bmatrix} + M^-(M_R) \begin{bmatrix} \rho_R \\ \rho_R u_R \\ \rho_R v_R \\ \rho_R H_R \end{bmatrix} \right] + \begin{bmatrix} 0 \\ p^f n_x \\ p^f n_y \\ 0 \end{bmatrix}$$

where a_f is the reference speed of sound; $M^+(M_L)$ and $M^-(M_R)$ are the left and right Mach number contributions to the face flux. M_L and M_R are the left and right normal Mach numbers multiplied by the matrices which evaluate the state conserved transport quantities. The face Mach number is given by $M_f = M^+(M_L) + M^-(M_R)$. H is the total enthalpy, $H = E + \frac{p}{\rho}$, and $E = e + 0.5(u^2 + v^2)$, where e is the internal energy.

The Rusanov flux is

$$\mathbf{F}_{\text{RUS}} = \frac{1}{2}(\mathbf{F}_L + \mathbf{F}_R) - \frac{1}{2}(|u_n| + a)(\mathbf{U}_R - \mathbf{U}_L)$$

where F_L and F_R is inviscid flux from left and right state, u_n is face normal velocity, a is speed of sound. Therefore, Inviscid face flux F^{inv} obtained is calculated for smooth flow while accounting for dissipative effects observed with strong shocks experienced during descent.

1.2.6 Viscous Fluxes and Turbulence Model

The viscous stress are calculated per unit area due to the velocity gradients,

Viscous stresses are calculated along x and r direction by equation 9 and equation 10.

$$\tau_{xx} = \frac{2}{3}\mu_{\text{eff}}(2u_x - v_r), \tag{9}$$

$$\tau_{rr} = \frac{2}{3}\mu_{\text{eff}}(2v_r - u_x), \tag{10}$$

$$\tag{11}$$

The shear stress is given by,

$$\tau_{xr} = \mu_{\text{eff}}(u_r + v_x) \tag{12}$$

where u_x, v_r are velocity components along x and r directions. μ being the effective viscosity $\mu_{\text{eff}} = \mu + \mu_{\text{turbulent}}$ with μ_{t} being turbulent viscosity term given by,

Effective viscosity:

$$\mu_{\text{eff}} = \mu + \mu_t, \quad \mu_t = \rho(0.4y)^2|\omega|$$

here, ρ is density, ω is scalar vorticity, flow variable and 0.4 being von karmann constant.

Heat flux, q is calculated as $\nabla\ T$, temperature gradient and k_{eff}, effective thermal conductivity as shown in below relation, [33]

$$\mathbf{q} = -k_{\text{eff}}\nabla T$$

1.2.7 Boundary Conditions

Boundary conditions at the wall of the geometry is used as : No slip wall condition is enforced i.e, no penetration shown in equation 13 and equation 14,

$$u = v = 0, \tag{13}$$
$$\tag{14}$$

Heat flux at wall q_w is given by equation 15,

$$q_w = k_g \frac{T_1 - T_w}{\Delta n} \tag{15}$$

where k_g is thermal conductivity of CO_2, T_1 temperature at first grid point adjacent to wall, T_w is wall temperature, $\triangle n$ is the distance in the normal direction from wall to the adjacent point.

At axis: zero normal gradient is imposed along the axis,

$$\frac{\partial \phi}{\partial n} = 0$$

here, ϕ is generic flow variable, n is direction normal to the axis of boundary. This ensures that the solution does not change while crossing the axis, when axi-symmetry is imposed.

Along the Far Field :

$$\rho = \rho_\infty(h), \quad T = T_\infty(h), \quad \mathbf{v} = \mathbf{v}_\infty$$

1.2.8 Initial Conditions

The initial conditions used for trajectory and flow parameters are defined below, it is assumed to be equal to the ambient atmospheric conditions as per mars GRAM model stated earlier in Table 3.

$$h(0) = h_0, \tag{16}$$
$$V(0) = V_0, \tag{17}$$
$$\gamma(0) = \gamma_0, \tag{18}$$
$$T(x, 0) = T_\infty(h_0). \tag{19}$$

1.2.9 TPS Thermal Response

The TPS energy equation is the rate of thermal energy increase inside the TPS given by equation 20,

$$\rho C_p \frac{\partial T}{\partial t} = \nabla \cdot (k \nabla T) + q_{\text{aero}} - \epsilon \sigma T^4. \tag{20}$$

where, T is the surface temperature of TPS, q_{aero} is aerothermal heat, C_p specific heat capacity at constant pressure, t is time, k is thermal conductivity of TPS material, σ is stefan-boltzmann constant, ϵ is surface emissivity.

Surface recession:

$$\dot{s} = \frac{q_{\text{aero}}}{\rho_s H_{\text{eff}}(h)}, \quad \Delta s = \dot{s} \Delta t \tag{21}$$

where s is surface recession rate, q_aero is aerothermal heat, ρ_s solid TPS density, $H_{eff}(h)$ effective heat of ablation as function of altitude and can be input into the model for correlation.

1.2.10 Mesh Deformation

Surface update:

$$\mathbf{x}_s^{n+1} = \mathbf{x}_s^n - \Delta s \mathbf{n}_s.$$

Interior nodes:

$$\mathbf{x}_{ij}^{n+1} = \mathbf{x}_{ij}^n - \Delta s \mathbf{n}_s (1 - \eta_j)^2.$$

where x_{s_n} is surface position at time step n, Δs is recession distance during the time step δt, n_x is x-component of the surface normal vector, x_{ij}^{n+1} is the updated surface position in n + *1* step, η_j is normalized computational coordinate in the wall-normal direction. *(1 -* η_j*)*^{2} keeps the outer boundary nearly fixed while smoothly deforming interior mesh. Further mesh discretization and evolution are discussed in detail in Section III(C).

2 Results and discussion

In this section, results of the simulation are presented. Trajectory results are presented, followed by aero-thermal and finally CFD results with mesh deformation. The trajectory is computed from altitude of 120 km above mars surface with initial conditions listed in Table 2. The entire timeline of the simulation is about 300 seconds from the point of re-entry. CFD is computed between 80 km altitude until the parachute open and especially when for mach greater than 3. The CFD enabled duration is of importance for TPS behavior and sizing therefore, rest of the events are not of concern. The parachute itself is set to deploy below Mach 2.2 and 16 km altitude, trajectory uses parameters set for the parachute in this regime. Final descent activities post parachute deployment and sky crane maneuver is ignored in this paper.

2.1 Trajectory results

The peak convective heating occurs at 80 second into the re-entry trajectory and followed by additional 100 seconds, parachute opens slowing the MSL till landing on

the surface. The parachute open for below Mach 2 (at Mach 1.7 for MSL) and about 16 km altitude as shown in figure 3(a) and figure 3(b). The maximum dynamic pressure load on the belly of the geometry during re-entry is at 90 seconds with approximately 12 kPa as shown in figure 3(c) of force thus marking, the maximum deceleration point during re-entry. At the same time instant, maximum G-load is experienced at approximately 13g's as shown in figure 3(d).

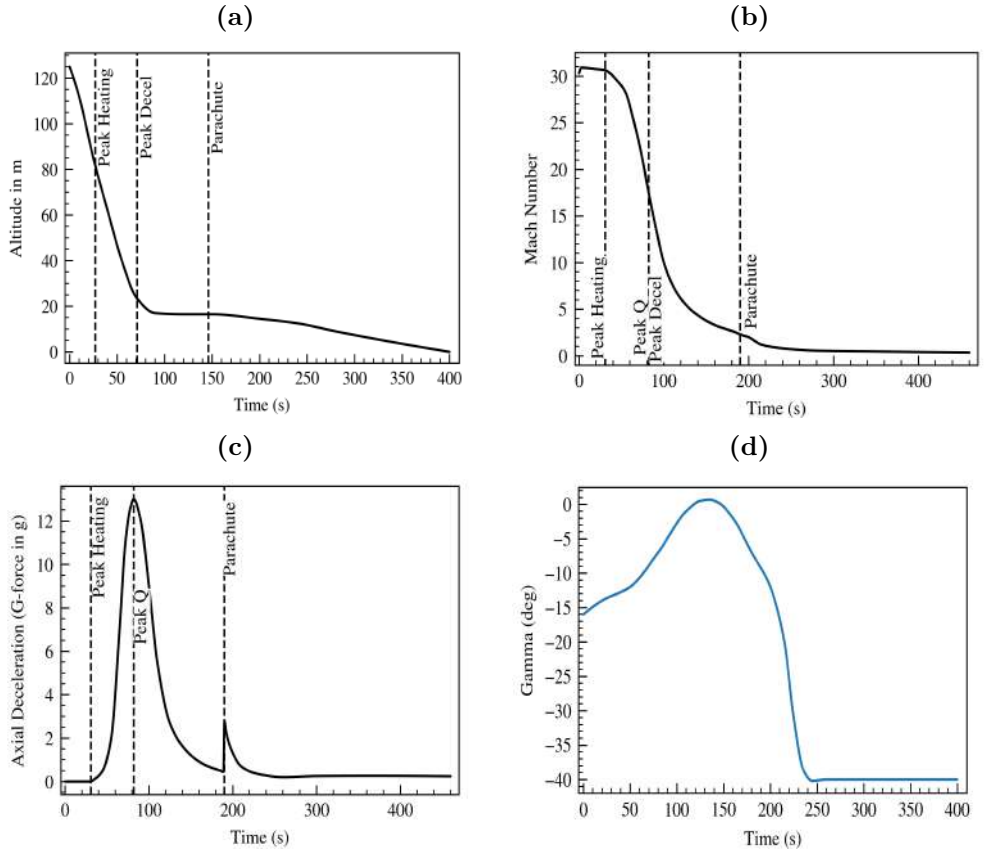


Fig. 3: Trajectory and mass telemetry results: (a) altitude, (b) Mach number, (c) force in Gs, and (d) flight path angle, versus time.

At the beginning of the re-entry descent, the angle of attack is assumed for a cold start at 0 deg. From 80 km altitude, the Angle of attack assumes the initial condition of MSL at 16 degrees until the parachute opening event takes place, reducing it to 40 deg as shown in figure 6. During MSL descent 79 m/s was measured at altitude of 1.6 km from mars surface, powered descent segment reduced it further to safe landing speeds however it is not implemented in this study[41].

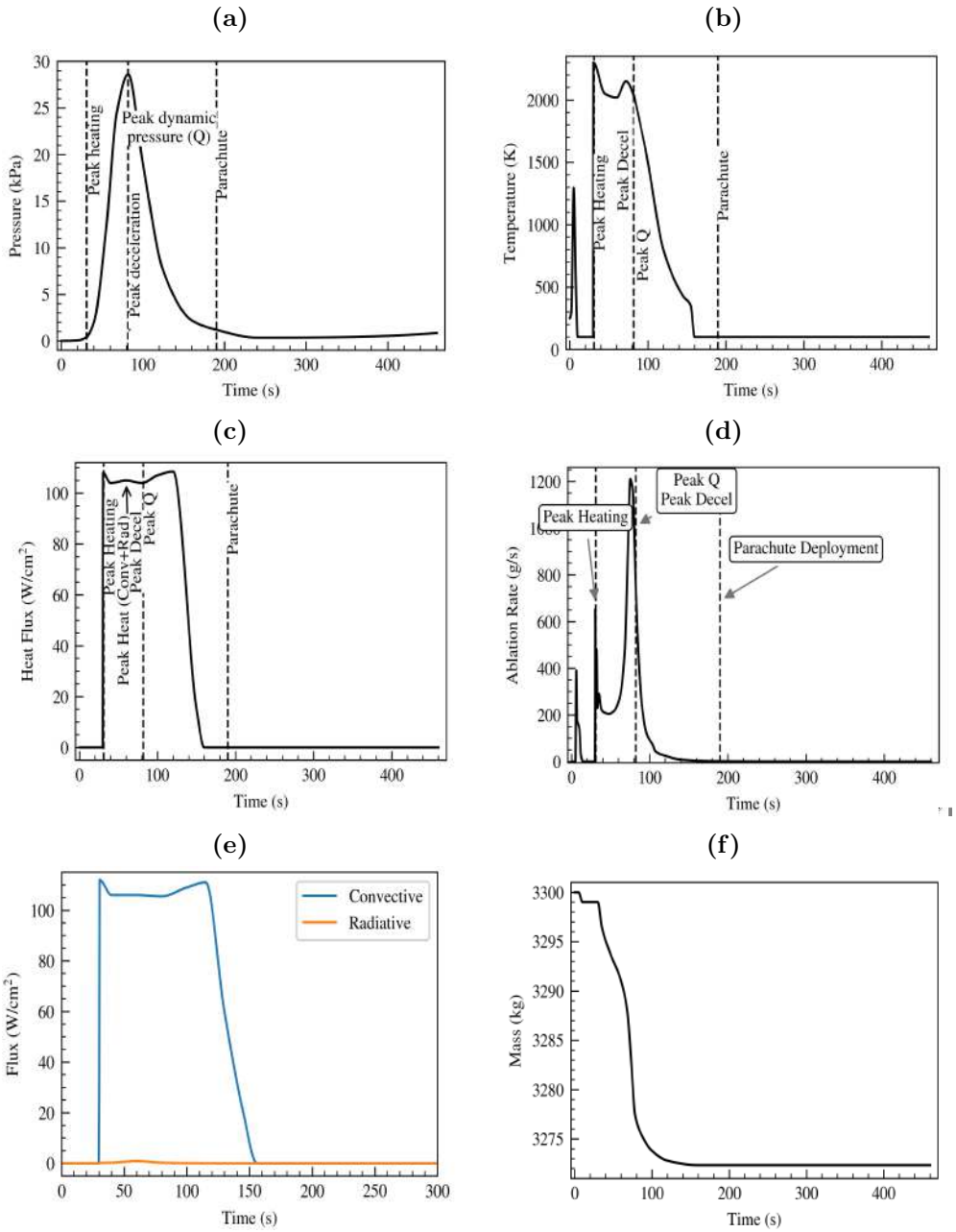


Fig. 4: Aero-thermal results: (a) pressure, (b) temperature, (c) heat flux, (d) ablation rate, (e) convective and radiative flux, and (f) mass, versus time.

2.2 Aero-thermal results

The peak pressure as shown in figure 4(a) coincides with the peak dynamic pressure and maximum deceleration during re-entry descent as shown in comparison with figure 3. However, peak heating occurs slightly earlier around 60-90 second into the re-entry descent as shown in figure 4(b), figure 4(d) and figure 4(e). The heating regime is not a unique event during the descent. Initially, rapid rise is observed due to the turbulent flow regime where heating of TPS surface takes place. Secondly, when the maximum turbulence flow is experienced, maximum heating occurs around 90 seconds as shown in figure 4. The radiative flux in figure 4(e) is under-predicted due to 2D equivalent geometry being considered for radiative calculations instead of ray tracing on 3D geometry. As shown in Figure 5,

- 0–60 s: Ratio $\approx 1.0 \rightarrow$ heating is essentially laminar, momentum-thickness Reynolds number (Retheta) defined as $Re_\theta = \frac{U\theta}{\nu}$ almost zero, here U is freestream velocity, ν is viscosity and θ is momentum thickness.
- 60–90 s: Rapid rise $\rightarrow$ onset of turbulence boosting heating. An increase in reynolds number is seen purely due to an increase in free-stream density. The curve crossing the threshold is close to the peak heating event. That crossing implies the boundary layer is predicted to become turbulent during the most thermally demanding part of entry, which is important because turbulence tends to increase convective heating and wall shear.
- Peak near 90 s: Ratio $\approx 2.0 \rightarrow$ turbulent heating is about $2\times$ the laminar heating at the peak with the free-stream density also contributing to this.
- 90–155 s: Decay $\rightarrow$ turbulent augmentation reduces as flow conditions change due to lower Reynolds number due to deceleration of the MSL, however, the decay is not too steep due to free-stream density increase. Physically, this is when the vehicle is deep enough that density is significant but still velocity is large enough that aerodynamic forcing is strong that can maximize Reynolds number based transition indicators.
- Greater than 200 s : Reynolds number falls and then levels off below the threshold. This reflects the regime where velocity is dropping quickly and the reduction in speed and associated boundary-layer edge conditions begins to outweigh further density increases.By the time the parachute opens, the curve is well below the transition threshold, indicating that the analysis is treating the boundary layer as laminar again. Since the transition is short and not long sustained, it is possible to understand that only portions of the heat shield become turbulent.

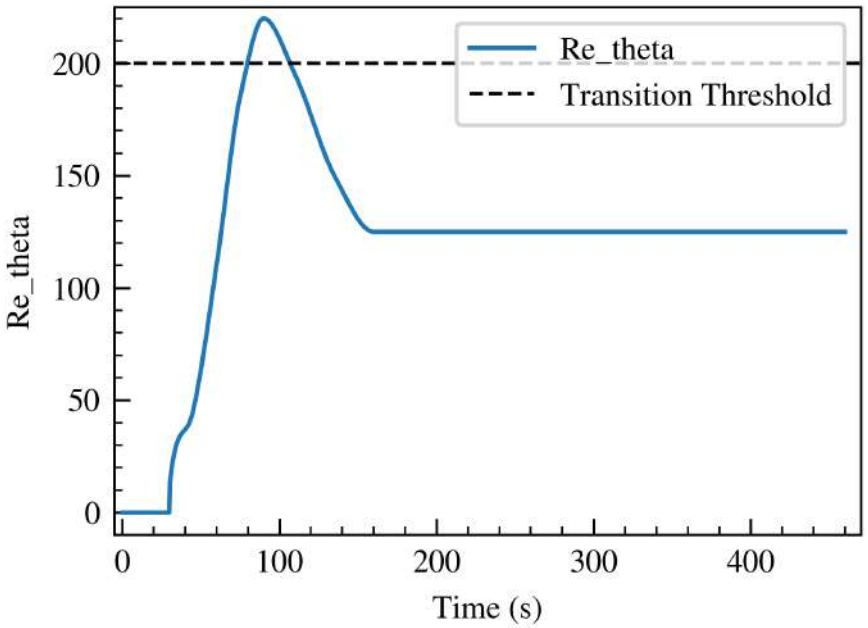


Fig. 5: Momentum thickness Reynolds number (Re_θ) vs flight time

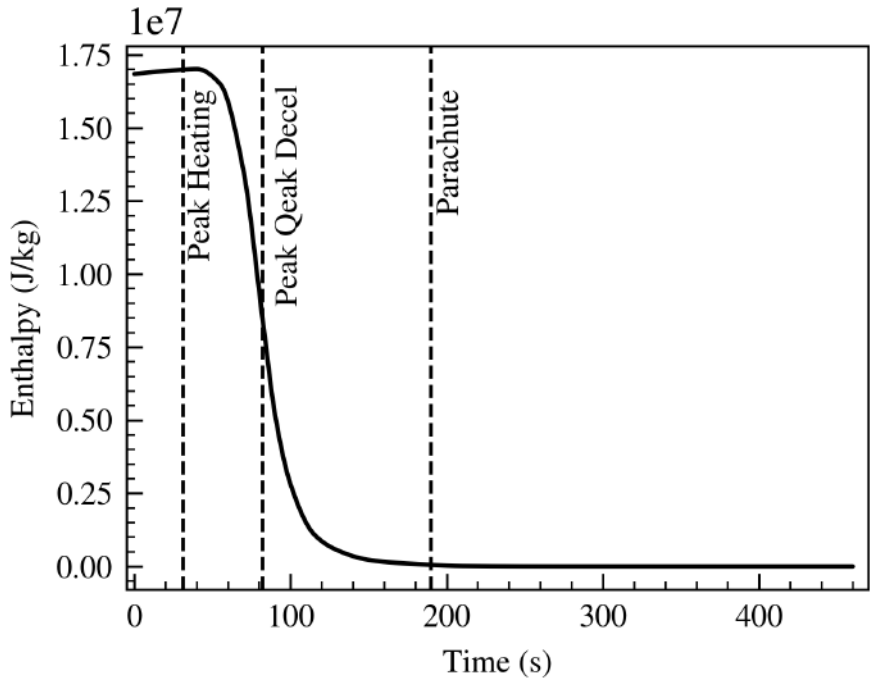


Fig. 6: Re-entry Simulation Enthalpy vs flight time

In Figure 6 plots the time history of total specific enthalpy along the Mars entry trajectory. During the early portion of entry, the freestream enthalpy remains near its upper asymptote because the vehicle is still essentially ballistic in a tenuous environment. Freestream density is insufficient to produce substantial drag flow field, while strongly compressible, is not yet forcing rapid conversion of the bulk kinetic energy into irreversible internal energy. Around the peak heating marker, total enthalpy is still near its maximum in-fact shows the trend to increase slightly. The peak convective heating typically occurs while the vehicle is still hypersonic and the kinetic energy level is high, but density has risen enough to produce strong compression and heat transfer in the shock layer. Freestream density has increased enough that the boundary layer is no longer diffusion-limited by rarefaction and the shock-layer compression can sustain large heat-transfer driving potentials. The steep decline between roughly the maximum dynamic pressure and Peak Decel markers indicates the period where aerodynamic braking is strongest and kinetic energy is being converted most aggressively into aerothermal loading. This interval corresponds to the regime in which the coupled effects of rising density and still-elevated Mach number maximize the global conversion of ordered kinetic energy into entropy. The MSL decelerates quickly and the flow-field's capacity to generate thermal and mechanical loads is at its highest here. While MSL simultaneously transitions toward lower Mach numbers where compressibility-driven heating diminishes. By the time the trajectory reaches the Parachute marker, total enthalpy has dropped by orders of magnitude and curve has nearly flattened. This reflects that the vehicle is now in a much lower-energy, lower-Mach regime where additional aerodynamic energy dissipation continues but at a far slower rate. From an EDL design standpoint, this is precisely the desired sequencing for parachute inflation and canopy load management. They are only viable once the freestream energy has been reduced to levels consistent with structural and material limits.

Overall, $\approx$ estimated 27 kilogram of TPS material is lost during the re-entry descent as evident from figure 4(f). The contribution of heat fluxes is majorly convective which remains high from 40 second till 90 second and then radiative flux which peaks at 60 seconds specifically in the hypersonic turbulent regime into the re-entry descent. A maximum of 115 W/m^2 is observed as shown in figure 9. The peak heating therefore must be considered at the time of high radiative flux with around 70 seconds into the descent along with constant 100 W/cm^2 convective flux configuration during this phase as evident from figure 4(c).

2.3 CFD visualization

The flow solver employs a two-dimensional, body-fitted, structured mesh in (i, j) topology, representing an axisymmetric meridional slice of the entry capsule. Mesh coordinates are stored at grid nodes $(X_{i,j}, Y_{i,j})$ and the governing equations are advanced on cell-centered control volumes, yielding $(N_i - 1) \times (N_j - 1)$ finite volumes for a mesh of $N_i \times N_j$ nodes (in the present implementation, $N_i = \texttt{GRID_NI} = 70$ and $N_j = \texttt{GRID_NJ} = 120$) as shown in Figure 7

2.3.1 Surface representation

The inner boundary is defined directly from the vehicle outer mold line (OML). A high-resolution sphere–cone profile is first generated and then re-parameterized to the CFD surface resolution. Specifically, a dense set of coordinates $(x(s), r(s))$ is constructed by concatenating a spherical nose arc and a conical frustum. The arc-length distribution is computed as

$$s_k = \sum_{m=1}^{k} \sqrt{(x_m - x_{m-1})^2 + (r_m - r_{m-1})^2}, \tag{22}$$

and the final OML discretization is obtained by interpolation to a uniform arc-length grid, producing surface arrays $\{x_{s,i}, r_{s,i}\}_{i=1}^{N_i}$.

2.3.2 Outer boundary and algebraic interior blending

The far-field boundary is constructed by offsetting the surface along its local outward normal direction. Surface tangents are approximated via centered differences and normalized to obtain unit normals (n_x, n_r),

$$\mathbf{t}_i = \frac{(\partial x/\partial i,\ \partial r/\partial i)}{\|(\partial x/\partial i,\ \partial r/\partial i)\|}, \qquad \mathbf{n}_i = (-t_{r,i},\ t_{x,i}), \tag{23}$$

followed by an outward offset distance d_i. In the code, d_i varies monotonically from a prescribed nose standoff (≈ 1.8 m) to an expanded wake extent (up to $5\times$ the standoff) to accommodate downstream gradients. The outer boundary coordinates are then

$$x_{o,i} = x_{s,i} + n_{x,i}\, d_i, \qquad r_{o,i} = r_{s,i} + n_{r,i}\, d_i. \tag{24}$$

To enforce physical admissibility near the axis of symmetry, the radial coordinate is constrained to be non-negative on the outer boundary (i.e., $r_{o,i} \leftarrow \max(r_{o,i}, 0)$), and the nose point is explicitly anchored on the axis. Interior nodes are created by algebraic blending between the wall and far-field boundaries. Let $\eta_j \in [0, 1]$ denote the wall-normal computational coordinate. A power-law clustering function

$$s(\eta) = \eta^p, \qquad p = 2.5, \tag{25}$$

is used to concentrate points near the wall ($\eta \to 0$), improving resolution of near-surface gradients. The interior mesh is defined as

$$X_{i,j} = x_{s,i}\,(1 - s_j) + x_{o,i}\, s_j, \qquad Y_{i,j} = r_{s,i}\,(1 - s_j) + r_{o,i}\, s_j, \tag{26}$$

where $s_j = s(\eta_j)$. Although the generator is labeled mesh generator elliptic, the current implementation uses the above algebraic normal-offset construction.

2.3.3 Geometric metrics used by the solver

At each update, the solver recomputes standard geometric metrics required for flux integration. Cell centroids are evaluated by bilinear averaging of the surrounding

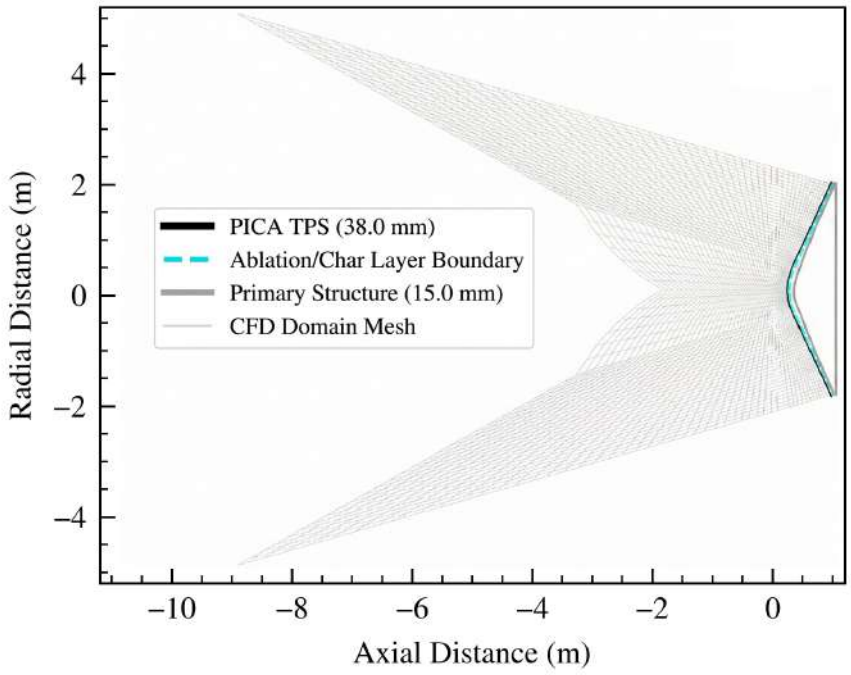


Fig. 7: Re-entry Simulation Geometry and axi-symmetric meshing

nodes. Cell volumes (areas in the meridional plane) are computed using a cross-product form consistent with a quadrilateral split into two triangles:

$$V_{i,j} = \frac{1}{2} \left| (\Delta x_1 \Delta y_2 - \Delta y_1 \Delta x_2) \right|, \tag{27}$$

with $\Delta x_1 = X_{i+1,j+1} - X_{i,j}$, $\Delta y_1 = Y_{i+1,j+1} - Y_{i,j}$, $\Delta x_2 = X_{i+1,j} - X_{i,j+1}$, and $\Delta y_2 = Y_{i+1,j} - Y_{i,j+1}$.

Face normals and face lengths are obtained from node differences along each index direction and normalized to provide outward unit normals (n_x, n_y) and metric terms (ΔA) for inviscid and viscous fluxes. Positive, non-degenerate cell areas are therefore a necessary condition for stable time integration, and the mesh construction enforces non-negative radii and monotone wall-normal spacing to reduce the risk of cell inversion.

2.3.4 Coupled mesh deformation with TPS recession

A distinguishing feature of the simulation is tight coupling between TPS recession and the CFD grid. At each physical time step, the TPS solver returns a recession increment along the surface. This recession field is (i) interpolated to the CFD wall-node count as needed and (ii) applied to the CFD mesh through a wall-normal displacement of

the node column adjacent to the wall. The deformation is damped away from the wall to preserve the far-field boundary and maintain mesh regularity:

$$\Delta \mathbf{x}_{i,j} = -\mathbf{n}_i \; \Delta r_i \; (1 - \eta_j)^2 \,, \tag{28}$$

where Δr_i is the local recession increment and η_j is the normalized wall-normal coordinate. After deformation, the body geometry is updated and the grid is regenerated using the same normal-offset and blending procedure. This regenerate-and-update strategy aims to maintain near-wall clustering and prevent progressive skewness accumulation that can occur under repeated purely Lagrangian deformation.

2.3.5 Mesh quality considerations

The structured topology and algebraic clustering provide inherently smooth connectivity and controlled point distribution, which are advantageous for robust finite-volume flux evaluation. In the present code-base, mesh "quality checks" are primarily enforced implicitly through: (i) geometric admissibility constraints (non-negative radial coordinates, anchored nose point), (ii) recomputation of positive cell areas/metrics required by the solver, and (iii) damping of deformation with distance from the wall to mitigate excessive skewness. Quantitative mesh quality metrics such as minimum angle, orthogonality, aspect ratio, or skewness are not explicitly reported by a dedicated routine in the current implementation. For archival-quality CFD verification, these metrics should be added and tracked across the trajectory, together with a mesh refinement study (e.g., varying N_i and N_j while monitoring integral quantities such as stagnation-point heat flux, integrated drag, and peak deceleration).

Figure 8(a) shows mach number distribution around the front head of the geometry at 16 km altitude. Since the flow is already in steady conditions, significant gradients are not observed. Figure 8(b) shows density distribution around the front head of the geometry at 16 km altitude. Since the flow is already in steady conditions, significant gradients are not observed. Figure 8(c) shows temperature distribution around the front head of the geometry at 16 km altitude. Since the flow is already in steady conditions, significant gradients are not observed. There is no heating of the TPS predicted at this altitude and flow field indicate globally uniform temperature of freestream flow around the geometry. Figure 8(d) shows Pressure distribution around the front head of the geometry at 16 km altitude. Since the flow is already in steady conditions, significant gradients are not observed. Figure 9 indicates TPS surface Temperature and Flux with respect to arc length distance from stagnation point around the geometry. The flux is not constant cross the cross-section but the surface temperature is uniform.

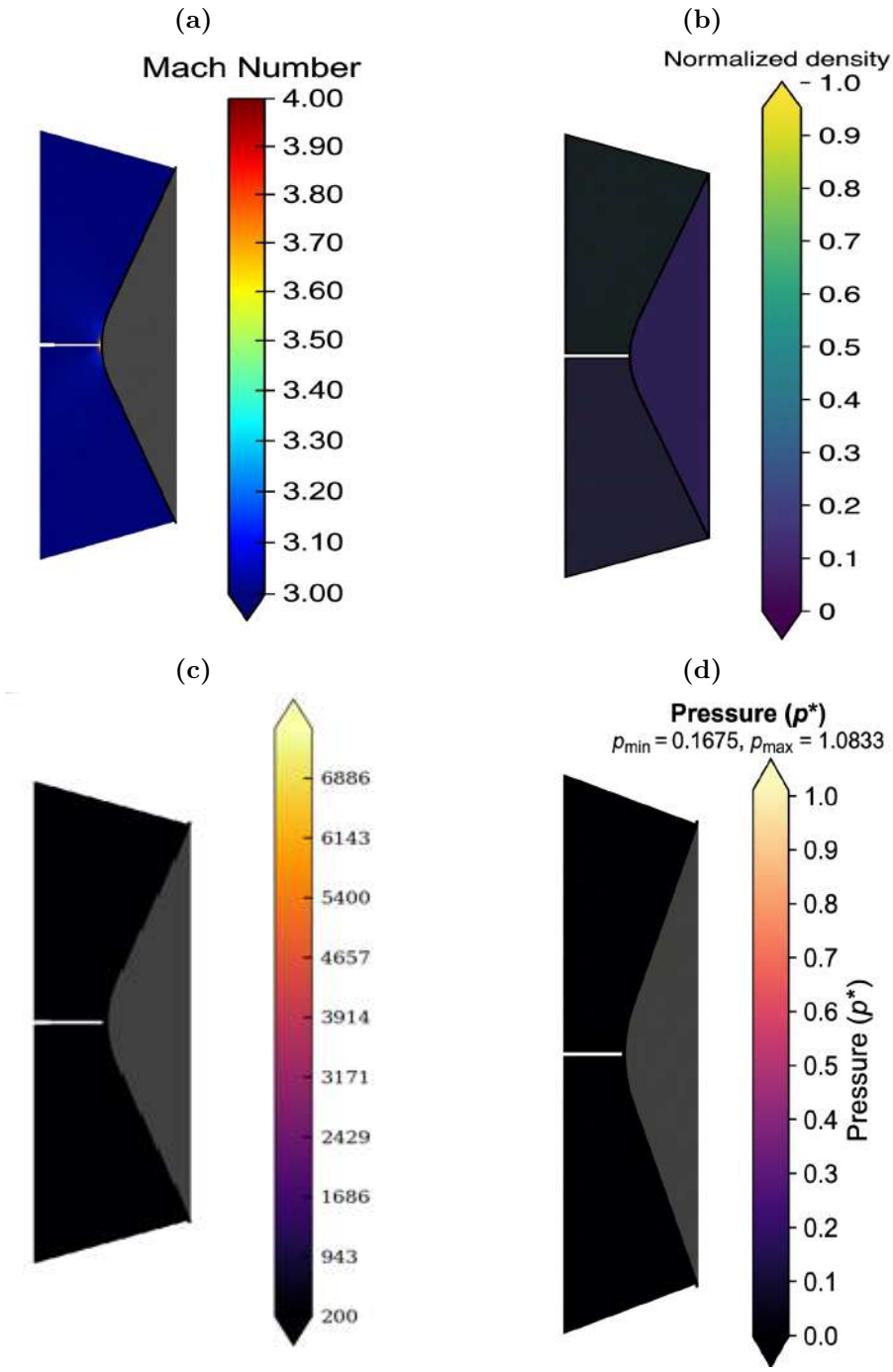


Fig. 8: CFD results at 16 km altitude: (a) Mach flow, (b) density, (c) temperature, and (d) pressure distributions.

2.4 Performance Metric

Using PC with Intel core i7, 4 GB GPU, 16 GB RAM, the following performance was observed as shown in Table 4. Total of 9000 second is required for the entire simulation and to generate outputs in the form of jpeg images in the dedicated folder in the local storage space of the PC. However, CFD solver consumes 99% of the time followed by meshing evolution.

3 Conclusion and Future work

Mars atmospheric entry remains a fundamentally coupled aero-thermo-structural problem, made especially acute by the CO_2-dominated, low-pressure Martian environment and the limited public availability of high-fidelity flight telemetry and validated atmospheric reconstructions. This combination continues to constrain the development and verification of predictive computational tools, while existing agency tool chains are often compartmentalized—requiring nontrivial external coupling to perform end-to-end analyzes spanning trajectory dynamics, high-enthalpy aerothermodynamics, radiative effects, and TPS sizing and ablation. To address this gap, this paper introduced JAYA, a tightly coupled, open-source framework that integrates trajectory propagation with CFD-based aerodynamic loading, fluid–structure interaction modeling, and TPS thermal response and ablation. The resulting architecture provides a unified pathway for consistently propagating atmospheric conditions through nonlinear flowfield loads into thermal and mass-evolution models, thereby enabling internally coherent predictions of both flight mechanics and TPS recession.

JAYA advances the trajectory while feeding aerodynamic forces and wall heat flux directly from the CFD solution. Then updates TPS recession and re-meshes every time

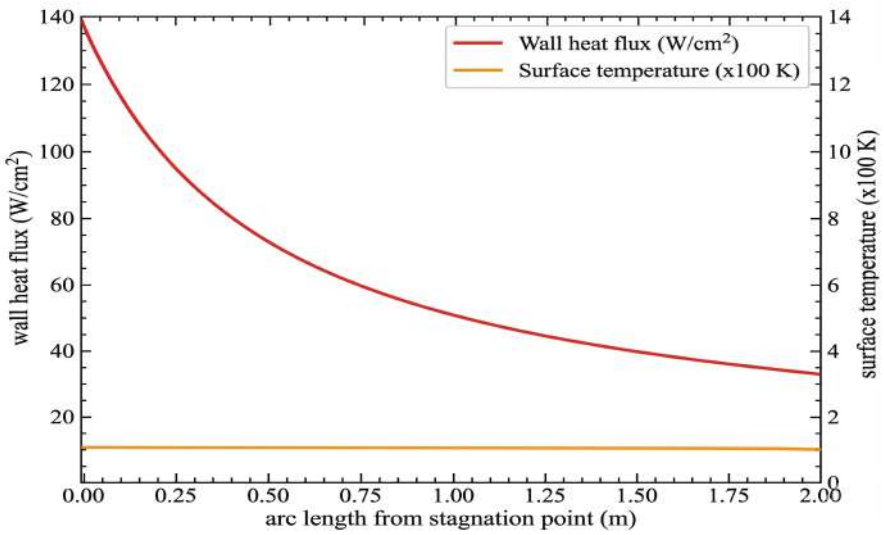


Fig. 9: TPS surface Temperature and Flux vs arc length distance from stagnation point

Table 4: JAYA performance profiling breakdown.

Component	**Time (s)**
Total loop time	8999.40
CFD solver time	8651.63
TPS/ablation time	84.08
Meshing/grid time	211.62
Trajectory/atmosphere time	7.82
I/O & plotting time	43.87

step. The near-wall nodes are displaced according to recession and a structured grid is regenerated via an elliptic-like interpolation with wall-normal clustering. Surface pressure and shear are integrated with a $2\pi r$ correction to obtain physically consistent axial forces for an axisymmetric capsule. Conductive heat flux is computed from near-wall temperature gradients and passed to a finite-rate TPS model including radiation to space and recession. Convective heating comes from CFD, radiative heating is calculated for the geometry with added possibility of calculation through correlation. AUSM and Rusanov-type dissipation are blended using a pressure-gradient sensor to stabilize shocks and strong gradients. A mixing-length eddy viscosity model is combined with an altitude-based turbulence switch and a Reynolds-based turbulent heating ratio. Granular timers separate CFD, TPS, meshing, trajectory, and I/O costs, enabling scaling and bottleneck identification. A self-contained architecture with trajectory, aerothermal, FSI - TPS coupling, mesh motion supports rapid development. It outputs 2D axisymmetric, multi-physics solution for future mars mission and trade off studies.

While the JAYA operates with a single gas species and single temperature field, high-fidelity hypersonic codes such as NASA's LAURA and the Data-Parallel Line Relaxation (DPLR) solver employ significantly more complex thermochemical models. This section contrasts the present formulation against these established codes in terms of governing equations, thermodynamic modeling and energy coupling. The key comparison parameters are shown in table 5 for LAURA, DPLR and JAYA. The framework is presently formulated in two-dimensional axi symmetry, which provides an effective basis for first-order analysis while offering a tractable platform for future extension toward fully three-dimensional phenomena. In this sense, the methodology is well suited for exploratory aerothermodynamic studies and design-space assessment, while also identifying a clear path toward the more extensive verification, validation and best-practice workflow development characteristic of mission-grade entry solvers. Overall, the work addresses an important step toward re-entry aerothermodynamic modeling by establishing a flexible and extensible framework that can support continued development in validation, uncertainty quantification and flight-quality predictive robustness.

Table 5: Comparison of hypersonic CFD formulations commonly used for TPS studies.

Feature	JAYA	LAURA	DPLR
Species transport	No	Yes	Yes
Finite-rate chemistry	No	Yes	Yes
Energy modes	1	1	2–3
Thermal equilibrium	Yes	Partial	No
EOS inversion	Scalar	Coupled	Multi-mode
Implicit time stepping	No	Yes	Yes
TPS coupling	Yes	Limited	Yes
Computational cost	Low–medium	High	Very high

Future work will focus on systematically advancing JAYA toward higher-fidelity and flight-relevant aerothermodynamic capability. A primary next step is the expansion of the Monte Carlo trajectory framework to more comprehensively sample initial flight-path angle and velocity variations, thereby strengthening the characterization of the full re-entry design space and its associated thermal environments. The TPS analysis will also be extended through refinement of the surface discretization and improved coupling between trajectory-dependent heat-flux predictions and spatially resolved temperature evolution, enabling more accurate assessment of non-uniform thermal loading. From a fluid-physics standpoint, the present simplified formulation provides a useful baseline for future incorporation of high-temperature transport, thermochemical non-equilibrium and more advanced shock-layer modeling consistent with hypersonic entry conditions. Extension beyond the current two-dimensional axisymmetric assumption will be an important direction, particularly for capturing inherently three-dimensional effects such as asymmetry, sideslip, wake and backshell interactions and geometrical protuberances. Additional work will further emphasize mesh-quality enforcement through rigorous orthogonality, skewness, and Jacobian controls, together with adaptive meshing and formal grid-convergence studies. Radiation modeling may likewise be improved by coupling the present framework with higher-fidelity non-equilibrium radiation tools, while transition and turbulence treatment can be enhanced through physics-based closures appropriate for transitional heating and separated wake flows. Finally, a major objective of future research will be the establishment of a broader verification, validation, and uncertainty-quantification framework so that the current research-oriented methodology can evolve toward a more robust predictive tool for flight-quality aerothermodynamic analysis.

Acknowledgments

References

[1] NASA Jet Propulsion Laboratory: Mars 2020 perseverance landing press kit.

Technical report, NASA Jet Propulsion Laboratory (2021). Accessed 2026-03-06. https://www.jpl.nasa.gov/news/press_kits/mars_2020/download/mars_2020_landing_press_kit.pdf

[2] Krenn, A.: Mars entry, descent, and landing (edl). Technical report, NASA Space Technology Mission Directorate (February 2025). Moon to Mars Architecture Workshops, February 2025. Accessed 2026-03-06. https://www.nasa.gov/wp-content/uploads/2025/02/iparch12-wp-mars-edl.pdf

[3] Edquist, K.T., Hollis, B.R., Johnston, C.O., Bose, D., White, T.R., Mahzari, M.: Mars science laboratory heatshield aerothermodynamics: Design and reconstruction. In: 44th AIAA Thermophysics Conference (2013). https://doi.org/10.2514/6.2013-2781 . NASA NTRS listing year 2013; often cited in later 2014 reference lists. Citation key retained from manuscript text. https://ntrs.nasa.gov/citations/20140000343

[4] Mahzari, M., Beck, R., Hwang, H., Monk, J., Morgan, J., Williams, J., Edquist, K.T.: Development and sizing of the mars 2020 thermal protection system. In: AIAA AVIATION 2022 Forum. American Institute of Aeronautics and Astronautics, ??? (2022). https://doi.org/10.2514/6.2022-3951 . AIAA Paper 2022-3951

[5] Euler, E.A.: Navigating the viking landers. (1977). NASA NTRS Document ID: 19770061576. https://ntrs.nasa.gov/citations/19770061576

[6] Polutchko, R.J.: Viking entry aerodynamics and heating. (1974). NASA NTRS Document ID: 19750012311. https://ntrs.nasa.gov/citations/19750012311

[7] Braun, R.D., Spencer, D.A., Kallemeyn, P.H., Vaughan, R.M.: Mars pathfinder atmospheric entry navigation operations. In: AIAA Guidance, Navigation, and Control Conference (1997). AIAA 97-3663; NASA NTRS Document ID: 19970026945. https://ntrs.nasa.gov/citations/19970026945

[8] Karlgaard, C.D., Korzun, A.M., Schoenenberger, M., Grover, M.R.: Mars insight entry, descent, and landing trajectory and atmosphere reconstruction. In: AIAA SciTech Forum (2020). NASA NTRS Document ID: 20200003204. https://ntrs.nasa.gov/citations/20200003204

[9] Desai, P.N., Knocke, P.C.: Mars exploration rovers entry, descent, and landing trajectory analysis. In: AIAA Atmospheric Flight Mechanics Conference and Exhibit (2004). AIAA 2004-5092; NASA NTRS Document ID: 20040095912. https://ntrs.nasa.gov/citations/20040095912

[10] Prince, J.L., Desai, P.N., Queen, E.M., Grover, M.R.: Mars phoenix entry, descent, and landing simulation design and modelling analysis. In: AIAA Guidance, Navigation, and Control Conference and Exhibit (2008). NASA NTRS Document ID: 20080033126. https://ntrs.nasa.gov/citations/20080033126

[11] Mendeck, G.F., Craig, L.: Mars science laboratory entry guidance. In: AIAA Atmospheric Flight Mechanics Conference (2011). NASA NTRS Document ID: 20110003649. Citation key retained from manuscript text. https://ntrs.nasa.gov/citations/20110003649

[12] Maddock, R.W., Dwyer-Cianciolo, A.M., Karlgaard, C.D., Korzun, A.M.: Insight entry, descent, and landing post-flight performance assessment. Journal of Spacecraft and Rockets (2021) https://doi.org/10.2514/1.A35023 . Originally circulated as a 2020 conference-era citation; normalized here to the journal record.

[13] Way, D.W., Dutta, S., Zumwalt, C.H., Blette, D.J.: Assessment of the mars 2020 entry, descent, and landing simulation. In: AIAA SciTech Forum (2022). https://doi.org/10.2514/6.2022-0421 . NASA NTRS Document ID: 20210024480. Citation key retained from manuscript text. https://ntrs.nasa.gov/citations/20210024480

[14] Wood, W.A.: Radiation coupling with the FUN3D unstructured-grid CFD code. In: 43rd AIAA Thermophysics Conference, p. 2741 (2012)

[15] Thompson, K.B., Johnston, C.O., Hollis, B.R., Lessard, V.R.: Recent improvements to the LAURA and HARA codes. In: AIAA AVIATION 2020 FORUM. American Institute of Aeronautics and Astronautics, Virtual Event (2020). https://doi.org/10.2514/6.2020-3030 . NASA NTRS Document ID 20205002031.

[16] Gnoffo, P.A.: An analysis of the LAURA code. Technical Report NASA/TP-1999-209015, NASA (1999)

[17] Jeng, M.: Aerothermodynamics and tps sizing of skip re-entry and aerocapture vehicles. Ph.d. dissertation, San Jose State University (2017)

[18] Dec, J.A., Braun, R.D.: An approximate ablative thermal protection system sizing tool for entry system design. In: 44th AIAA Aerospace Sciences Meeting and Exhibit. American Institute of Aeronautics and Astronautics, ??? (2006). https://doi.org/10.2514/6.2006-780

[19] Edquist, K.T., Dyakonov, A.A., Wright, M.J., Tang, C.Y.: Aerothermodynamic environments definition for the mars science laboratory entry capsule. In: AIAA Thermophysics Conference. American Institute of Aeronautics and Astronautics, ??? (2009). AIAA Paper 2009-3883. https://scispace.com/pdf/aerothermodynamic-environments-definition-for-the-mars-3m3iukbx4t.pdf

[20] Tang, C.: An introduction to DPLR. Technical Report / Presentation 20160010056, National Aeronautics and Space Administration, Ames Research Center, Moffett Field, CA, USA (2016). https://ntrs.nasa.gov/api/citations/20160010056/downloads/20160010056.pdf

[21] Braun, R.D., Powell, R.W., Engelund, W.C., Gnoffo, P.A., Weilmuenster, K.J., Mitcheltree, R.A.: Mars pathfinder six-degree-of-freedom entry analysis. Journal of Spacecraft and Rockets **32**(6), 993–1000 (1995) https://doi.org/10.2514/3.26720

[22] Brune, A.J., Tyler K. West, I., White, L.M.: Calibration probe uncertainty and validation for the hypersonic material environmental test system. Journal of Thermophysics and Heat Transfer **34**(2), 404–420 (2020) https://doi.org/10.2514/1.T5839

[23] Wright, M.J., Candler, G.V., Bose, D.: Data-parallel line relaxation method for the navier–stokes equations. AIAA Journal **36**(9), 1603–1609 (1998) https://doi.org/10.2514/2.586

[24] Wright, M.J., White, T., Mangini, N.: Data parallel line relaxation (DPLR) code user manual: Acadia – version 4.01.1. NASA Technical Memorandum NASA/TM-2009-215388, National Aeronautics and Space Administration, Ames Research Center, Moffett Field, CA, USA (2009). Document ID 20110006930. https://ntrs.nasa.gov/api/citations/20110006930/downloads/20110006930.pdf

[25] Thompson, J.F., Soni, B.K., Weatherill, N.P.: Numerical Grid Generation: Foundations and Applications. North-Holland, ??? (1985)

[26] Chen, Y.-K., Rasky, D.J.: Thermal response and ablation programs for TPS sizing computation. In: Proceedings of the Workshop on Aeroassist Technologies, Pasadena, CA (1997). NASA Technical Reports Server, Document ID 20020039735

[27] Connell, J.W., Smith, J.G., Hergenrother, P.M., Fred L. Banks, J., Kenney, M.E., Mabry, J.M.: Polyimide foams for aerospace vehicles. Technical Memorandum NASA/TM-2009-215620, National Aeronautics and Space Administration (2009). Accessed 2026-03-06. https://ntrs.nasa.gov/api/citations/20090007730/downloads/20090007730.pdf

[28] Braun, R.D., Manning, R.M.: Mars exploration entry, descent, and landing challenges. Journal of Spacecraft and Rockets **44**(2), 310–323 (2007) https://doi.org/10.2514/1.25116

[29] Wright, M.J.: Simulation of ablative response for Mars Science Laboratory heat shield. Journal of Spacecraft and Rockets **49**(6), 1065–1078 (2012)

[30] Grant, M.J., Brown, M.A., Crawley, E.F.: Framing challenges for the future of the aerospace industry. In: AIAA SPACE 2015 Conference and Exposition, p. 1894 (2015). https://doi.org/10.2514/6.2015-1894 . https://doi.org/10.2514/6.2015-1894

[31] Justh, H.L., Justus, C.G.: Mars global reference atmospheric model 2010 version: Users guide. Technical memorandum, National Aeronautics and Space Administration, Marshall Space Flight Center, AL, USA (February 2014). NASA Technical Memorandum, Document ID: 20140003184. https://ntrs.nasa.gov/citations/20140003184

[32] Reed, B.D.: Performance characterization of a low-power cylindrical hall thruster for the asteroid redirect robotic mission. Technical Memorandum NASA/TM-2014-216646, National Aeronautics and Space Administration (2014). Accessed 2026-03-06. https://ntrs.nasa.gov/api/citations/20140000343/downloads/20140000343.pdf

[33] John D. Anderson, J.: Computational Fluid Dynamics. McGraw-Hill, ??? (1995)

[34] Venkatapathy, E.: Ablation and thermal response of PICA. Journal of Spacecraft and Rockets (2004)

[35] Chen, Y.-K., Milos, F.S.: Ablation and thermal response program for spacecraft heatshield analysis. Journal of Spacecraft and Rockets **30**(4), 475–483 (1993)

[36] JPL/Caltech: The mars reconnaissance orbiter mission. Acta Astronautica (2005)

[37] Justus, C.G., Keller, V.F.: Mars-gram: Mars global reference atmospheric model. Technical memorandum, NASA (1996)

[38] Liou, M.-S.: A sequel to AUSM: AUSM+. Journal of Computational Physics **129**(2), 364–382 (1996) https://doi.org/10.1006/jcph.1996.0256

[39] Peters, J.: Hypersonic Aerothermodynamics and Thermal Protection Systems, (2016)

[40] Patel, R., Singh, A.: Fluid–structure interaction modeling of ablative heat shields for planetary entry. Aerospace Science and Technology **79**, 223–236 (2018)

[41] Karlgaard, C., Kutty, P., Shidner, J., Schoenenberger, M., Munk, M.: Mars entry atmospheric data system trajectory reconstruction algorithms and flight results. In: 51st AIAA Aerospace Sciences Meeting Including the New Horizons Forum and Aerospace Exposition (2013). https://doi.org/10.2514/6.2013-28